

## Article

# Flow Cytometry Characterization and Analysis of Glial and Immune Cells from the Spinal Cord

Lilian de Oliveira Coser, Manuela Tosi Comelis, Débora Elisa da Costa Matoso, Luciana Politti Cartarozzi  and Alexandre Leite Rodrigues de Oliveira \* 

Department of Structural and Functional Biology, Laboratory of Nerve Regeneration, Institute of Biology, University of Campinas, Campinas 13083-862, SP, Brazil; coser.lilian@gmail.com (L.d.O.C.); manuela1213@gmail.com (M.T.C.); d180535@dac.unicamp.br (D.E.d.C.M.); lpcarta@unicamp.br (L.P.C.)

\* Correspondence: alroliv@unicamp.br

**Abstract:** Several protocols have been developed with the aim of characterizing glial and immune cells from the central and peripheral nervous systems. However, a small number of these protocols have demonstrated the ability to yield satisfactory results following conventional isolation. Considering this necessity and the difficulties encountered in enzymatic and bead isolation, our work proposes a method for the isolation of glial and immune cells from the spinal cord utilizing a Percoll gradient. For this purpose, C57BL/6J spinal cords were dissected, and the lumbar intumescence was dissociated and subjected to a Percoll gradient centrifugation (70%, 50%, 37%, and 10%). Each layer was then separated and labeled for astrocytes (anti-GFAP, TNF- $\alpha$ , IFN- $\gamma$ , IL-10, IL-4), microglia (anti-CD45, CD11b, CD206, CD68, TNF- $\alpha$ , IFN- $\gamma$ ), and lymphocytes (anti-CD3, CD4, IFN- $\gamma$ , IL-4). The gate detections were mathematically performed by computational analysis utilizing the K-means clustering algorithm. The results demonstrated that astrocytes were concentrated at the Percoll 10/37 interface, microglia at the Percoll 37/50 layer, and lymphocytes at the Percoll 50/70 layer. Our findings indicate that astrocytes in healthy animals are putative of the A1 profile, while microglia and lymphocytes are more frequently labeled with M1 and Th1 markers, suggesting a propensity towards inflammatory responses. The computational method enabled the semi-autonomous gate detection of flow cytometry data, which might facilitate and expedite the processing of large amounts of data.

**Keywords:** flow cytometry; spinal cord; central nervous system; glial cells; immune cells



**Citation:** Coser, L.d.O.; Comelis, M.T.; Matoso, D.E.d.C.; Cartarozzi, L.P.; Oliveira, A.L.R.d. Flow Cytometry Characterization and Analysis of Glial and Immune Cells from the Spinal Cord. *Neuroglia* **2024**, *5*, 129–144. <https://doi.org/10.3390/neuroglia5020010>

Academic Editor: Stefania Ceruti

Received: 27 March 2024

Revised: 12 May 2024

Accepted: 13 May 2024

Published: 20 May 2024



**Copyright:** © 2024 by the authors. Licensee MDPI, Basel, Switzerland. This article is an open access article distributed under the terms and conditions of the Creative Commons Attribution (CC BY) license (<https://creativecommons.org/licenses/by/4.0/>).

## 1. Introduction

The homeostasis of the nervous system depends on the interplay between glial cells and neurons [1–3]. Astrocytes, which constitute up to 40% of all cells in the CNS, play important roles in synaptic regulation and plasticity, which are fundamental for the stability of the nervous system microenvironment. In addition, they maintain the homeostasis of extracellular fluids, ions, and transmitters [4], provide glucose for neurons [5], modulate blood flow [6], contribute to synaptic plasticity [7], and thus, influence neuronal circuit function and animal behavior [8]. Several variants have been described, as well as subtypes found only in humans [9]. Different areas of the brain and spinal cord have specialized astrocytes that develop specific functions. In the spinal cord, for example, fibrous astrocytes are found in the white matter, protoplasmic astrocytes populate the gray matter, and perivascular astrocytes are fundamental to the establishment of the blood–brain barrier [2]. There is a polarization gradient in the profile of these glial cells, and concerns have been raised about the oversimplification of binary classifications [10]. However, in the context of a lesion or disease, astrocytes can develop neurotoxic or neuroprotective roles and are, therefore, classified as A1 when pro-inflammatory and A2 when anti-inflammatory. A1 astrocytes secrete IL-1 $\alpha$ , TNF, and C1q, thus contributing to the exacerbation of an inflammatory process that can lead to tissue remodeling but also to neuronal death. In

contrast, A2 astrocytes are protective, secreting neurotrophic factors and anti-inflammatory cytokines [11,12]. Depending on the inflammatory process that triggers A1 astrocyte activation, the NF $\kappa$ B pathway may induce the secretion of neurotoxic molecules, leading to neuronal damage and apoptosis. In contrast, A2 polarization can be controlled by the Stat3 pathway, allowing neuronal survival and tissue repair [11,13–15].

In this context, microglia can also polarize into pro- and anti-inflammatory profiles, namely M1 and M2. These two phenotypes are known as the classical (M1) and alternative phenotype (M2), where M1 activation is induced by IFN- $\gamma$  and LPS, producing classical cytokines such as TNF- $\alpha$ , IL-6, IL-1 $\beta$ , IL-12, and CCL2. In addition, M1 microglia express NADPH, MHC-II, key integrins such as CD11b and CD11c, and costimulatory molecules such as CD36, CD45, and CD47. Alternative activation upregulates anti-inflammatory cytokines such as IL-4 and IL-13 and produces IL-10 and TGF- $\beta$  along with the growth factors IGF-1, CSF-1, NGF, BDNF, and GDNF. In addition, M2 macrophages express CD206, FIZZ1, Chil3, and Arg1 [16–20].

Microglial activation occurs after infection, disease, or trauma and leads to morphological and physiological changes, including increased motility, phagocytosis, and cytokine secretion. Furthermore, the mixed profile of M1/M2 and intermediate states has been found in different cases [21–24]. On the one hand, M1 microglia represents a pro-inflammatory profile in response to TNF- $\alpha$  and IFN- $\gamma$ , which has a role in phagocytosis, its response to pathogens, and ROS release [25]. On the other hand, M2 microglia have an anti-inflammatory profile that acts to downregulate inflammation and has a neuroprotective profile in the CNS [25,26].

Glial and immune responses are hallmarks after CNS and PNS lesions or diseases, including spinal cord injury (SCI), multiple sclerosis (MS), and amyotrophic lateral sclerosis (ALS). Recent studies in patients have shown that the acute phase after SCI is predominantly pro-inflammatory, containing IBA-1- and CD68+-expressing cells corresponding to M1 microglia and macrophages at the lesion site [27,28]. Astrocytes (GFAP+) polarized to a pro-inflammatory state have also been observed in ALS patients following microglial activation, contributing to neuronal death [29,30]. In MS patients, glial responses are critical for disease progression once microglia exacerbate T-cell antigen presentation and contribute to disease progression [31–33].

The reactive profile after SCI increases scarring at the site of injury and, in some cases, inhibits plasticity and regeneration. Activated A1 astrocytes induce apoptosis, destabilize the synapses, and exhibit reduced phagocytic properties. They also prevent oligodendrocyte differentiation, even leading to the apoptosis of such myelinating cells, which may contribute to further axonal degeneration [11]. A2 astrocytes show the opposite role by increasing the availability of neurotrophic factors, resulting in neuroprotection [11,13].

Importantly, the astroglial reaction is closely influenced by prior microglial activation and its response to damage. Thus, as fundamentally the first responders to injury, microglial cells quickly perceive alterations in the CNS milieu [34]. The phagocytic activity of such cells correlates with the strong upregulation of lysosome-associated glycoprotein CD68, which can be used as a marker of activation. Upon pro-inflammatory polarization (M1 profile), they contribute to the build, mostly by astrocytes, of a physical barrier around the lesion site, thus hampering axonal regrowth and contributing to the permanent loss of function and perpetuation of the inflammatory process [35–39]. The M2 profile, on the contrary, contributes to the resolution of the lesion and inflammatory response. Thus, the phenotyping of microglial cells and their polarization is an important tool for prospecting new treatments following CNS injury. Following microglial activation, the release of damage-associated molecular patterns (DAMPs) further recruits immune cells, such as neutrophils, monocytes, and other adaptive immune cells, to the site of injury [40]. Specially, macrophages have an important role in the resolution of the inflammation process, alongside with the phagocytic function, as they produce growth factors, cytokines, and chemokines [41,42]. Lymphocytes are also at play after injury, as they regulate macrophage function [43,44].

The identification and characterization of glial and immune cell polarization *in situ* is a challenging endeavor due to the need to assess multiple markers. In addition, high-throughput evaluation in tissue sections is not possible due to the limited volume of tissue and cells that can be evaluated. Furthermore, the evaluation of the interaction of microglia with astrocytes is crucial for the best understanding of the inflammatory process, but for this to occur simultaneously, multiple evaluations are required.

High-throughput methods that provide the refined profiling of glial and lymphocyte polarization could help to identify new therapeutic agents, such as neuroprotective, anti-inflammatory, and antioxidant drugs. Reactive glial cells were found after the SCI, crush, and avulsion of spinal nerves, which is a frequent event after brachial and lumbosacral plexus trauma caused by high-energy accidents [26,45]. Such lesions lead to permanent changes in motor, sensory, and autonomic functions of the spinal cord [46]. They also result in motoneuron degeneration and astroglial and microglial persistent activation, leading to chronic pain [26,45,47,48].

Herein, we propose a new approach based on flow cytometry to thoroughly evaluate the polarization of astrocytes, microglial cells, and lymphocytes in health and disease. The results demonstrate a natural predisposition of such cell types to polarize towards a pro-inflammatory profile, which, in turn, may be useful for evaluating new approaches to treat injury and neurodegenerative diseases. In addition, to facilitate the analysis of large datasets, we propose a computational method to semi-automatically find appropriate gates based on the machine learning algorithm K-means [49,50]. The goal of this algorithm is to partition the data into *k* clusters of equal variances, where each observation belongs to the cluster with the closest mean. The proposed new mathematical method shows comparable accuracy (86% of events) to the manual conventional software gating process. In addition, it offers greater scalability and computational efficiency due to its semi-automatic nature [49,50].

## 2. Materials and Methods

### Animals

Eight-to-twelve-week-old female C57BL/6J and CX3CR1-EGFP mice were used for the flow cytometry analysis ( $n = 3$  each strain). All experiments followed the standards for ethics in animal experimentation preconized by the National Council for Animal Experimentation Control (CONCEA—Brazil) and were approved by the Institutional Ethics Committee on the Use of Animals (CEUA/IB/UNICAMP, protocol n°5327-1/2019). Animals were maintained at the animal facility of the Laboratory of Nerve Regeneration—LRN, Institute of Biology, University of Campinas, under 12 h light–dark cycles, with water and food *ad libitum*.

Spinal cords from CXCR-EGFP animals [51] were also used in part of the experiments to confirm the efficiency of the cell separation method, which was analyzed by immunofluorescence microscopy (Leica DMB5500, Leica, Wetzlar, Germany). For flow cytometry and immunofluorescence analysis, we considered  $n = 3$  for each analysis as a reproducible standard. In this case, a control group was not necessary since we utilized healthy animals in our method.

### Flow cytometry

Animals were euthanized with xylazine (König, Argentina, 15 mg/kg) and ketamine (Fort Dodge, IA, USA, 300 mg/kg) according to humane endpoints to avoid pain and suffering. Then, they were perfused with phosphate-buffered saline (PBS), and their spinal cords were dissected out under a surgical microscope (DFV Vasconcelos, São Paulo, Brazil); the lumbar intumescence was obtained for analysis. The tissue was mechanically dissociated and passed through stainless-steel meshes of 140  $\mu\text{m}$  and 70  $\mu\text{m}$ . The cell suspension was centrifuged at  $400 \times g$  for 5 min at 4 °C, followed by resuspension in 70% Percoll solution (Sigma, Livonia, MI, USA). Also, 50%, 37%, and 10% Percoll solutions were carefully added in layers. Another centrifugation at  $400 \times g$  for 30 min at 4 °C without

brake was carried out. The myelin was removed, and every layer interface was collected in separate tubes, i.e., 10/37, 37/50, and 50/70.

Ex vivo stimulation with PMA (Phorbol 12-myristate 13-acetate), brefeldin A, and ionomycin (Sigma, USA) was carried out in each fraction for intracellular labeling. For this, each tube with a different layer interface was centrifuged at  $400\times g$  for 10 min at  $4\text{ }^{\circ}\text{C}$  for pellet obtention. Then, the pellet was resuspended in 1 mL of supplemented DMEM (10% heat-inactivated fetal bovine serum) containing penicillin/streptomycin (1 mg/mL, Vitrocell, Campinas, Brazil) in 24 well plates and 5  $\mu\text{L}$  of PMA (50 ng/mL), 5  $\mu\text{L}$  of brefeldin A (1  $\mu\text{g}/\text{mL}$ ) and 5  $\mu\text{L}$  of ionomycin (250 ng/mL) were added to the cell medium to block cytokine secretion and allow intracellular labeling for 3 h at  $37\text{ }^{\circ}\text{C}$  (5%  $\text{CO}_2$ ). In sequence, the cells were centrifuged at  $400\times g$  for 10 min at  $4\text{ }^{\circ}\text{C}$  for pellet obtention. The supernatants were removed, and the pellet was resuspended in 200  $\mu\text{L}$  of PBS-BSA-A (PBS—Bovine Serum Albumin 0.1%—Sodium Azide 0.5%). According to the antibody panel (Table 1), 50  $\mu\text{L}$  of each layer was added to the 96-well plate, which was divided into wells 1–3 for the 10/37 layer interface, wells 4–6 for the 37/50 layer, and wells 7–8 for the 50/70 layer.

**Table 1.** Antibody panels used to analyze the cell phenotypes.

SAMPLE	FITC	PE	PERCP	PE-CY7	APC	APC-CY7
1	-	-	-	-	-	-
2	GFAP	IL-10	-	-	IL-4	-
3	GFAP	-	TNF- $\alpha$	IFN- $\gamma$	-	-
4	-	-	-	-	-	-
5	CD45	IL-10	-	CD206	-	CD11b
6	CD45	-	TNF- $\alpha$	-	CD68	CD11b
7	-	-	-	-	-	-
8	CD4	-	-	IFN- $\gamma$	IL-4	CD3

Cells were incubated with the extracellular antibodies anti-CD45-FITC, anti-CD206-PE-Cy7, anti-CD68-APC, anti-CD11 b-APC-Cy7, anti-CD4-FITC and anti-CD3-APC-Cy7 (Biolegend, San Diego, CA, USA) and labeled with 0.5  $\mu\text{L}$  live/dead for 30 min at  $4\text{ }^{\circ}\text{C}$  (Invitrogen, Life, Waltham, MA, USA) diluted in PBS-BSA-A. Each layer was labeled with the respective antibodies for phenotype analysis, and a cell without labeling was performed for each layer. Next, the cells were washed with 150  $\mu\text{L}$  of PBS-BSA-A at  $400\times g$  for 10 min at  $4\text{ }^{\circ}\text{C}$ , followed by fixation for 20 min at  $4\text{ }^{\circ}\text{C}$  with 150  $\mu\text{L}$  of a fixed buffer (kit True-Nuclear Transcription Buffer Set; Biolegend, San Diego, CA, USA), following the manufacturer's instructions.

Cells were then washed with 150  $\mu\text{L}$  of PBS-BSA-A to initiate the intracellular labeling, in which the cells were permeabilized with 120  $\mu\text{L}$  of a permeabilization buffer for 20 min at  $4\text{ }^{\circ}\text{C}$ , followed by intracellular labeling with anti-GFAP-FITC, anti-IL-10-PE, anti-TNF- $\alpha$ -PE-Cy5, anti-IL-4-APC, and anti-IFN- $\gamma$ -PE-Cy7 (Biolegend, San Diego, CA, USA) diluted in a permeabilization buffer. Then, the cells were incubated at  $4\text{ }^{\circ}\text{C}$  overnight.

Afterward, cells were washed twice with a permeabilization buffer with  $400\times g$ —10 min— $4\text{ }^{\circ}\text{C}$  centrifugation and fixed with 200  $\mu\text{L}$  of a fixed buffer (Biolegend, San Diego, CA, USA) for 20 min at  $4\text{ }^{\circ}\text{C}$ . Cells were examined with the NovoCyte Flow Cytometer (ACEA biosciences, San Diego, CA, USA) and the data were analyzed by the NovoExpress software (version 1.6.2) considering a minimum of 10,000 events (Figure 1). Samples without labeling were used to set the position of each quadrant to determine the positive percentage of each marker. Also, a single-cell analysis was performed to eliminate the doublets before the analysis of cell phenotype (Figure 2). All experiments were carried out in triplicate.



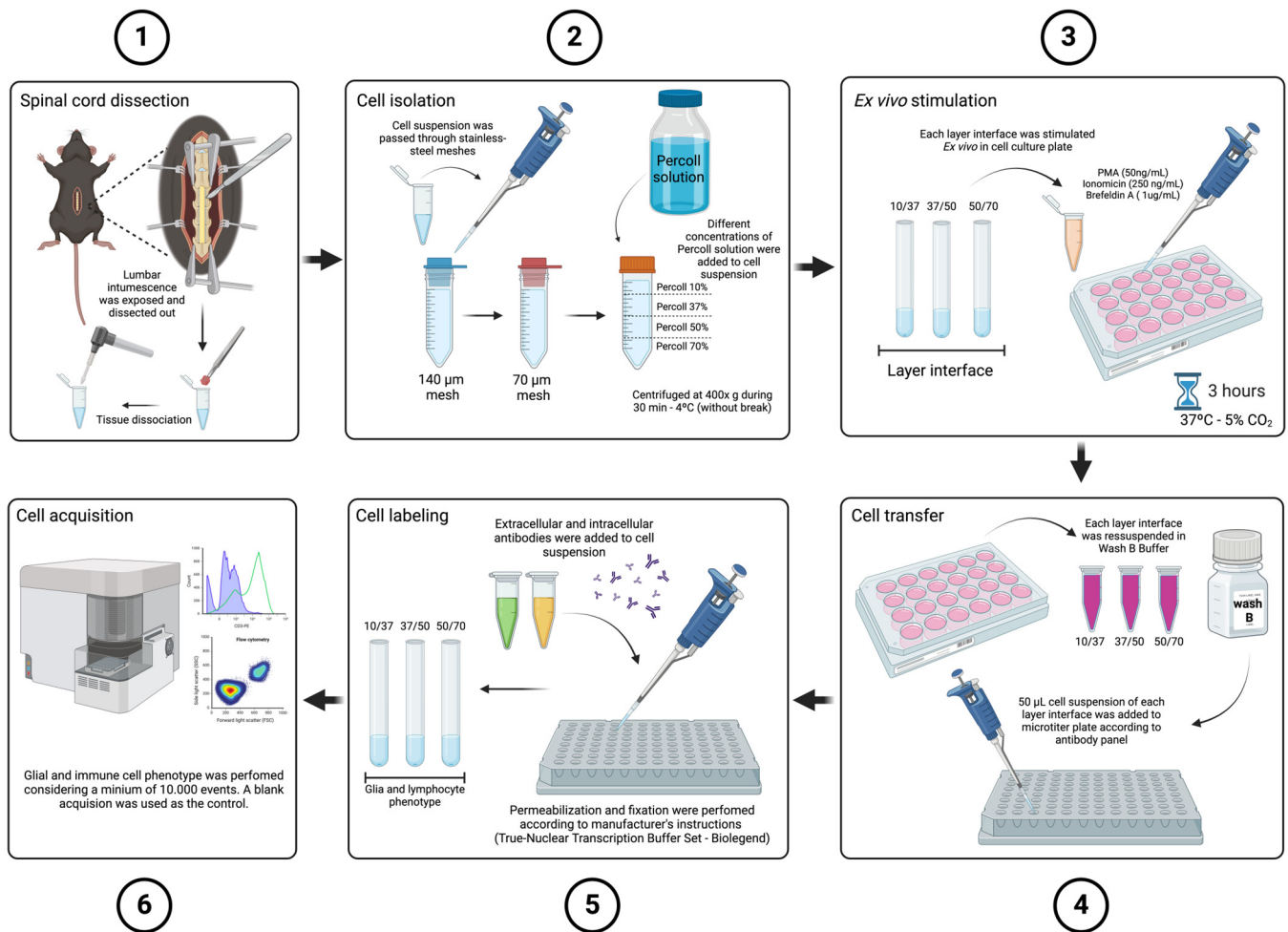


**Figure 1.** Protocol design. C57BL/6J animals were euthanized, and the spinal cord was extracted. The lumbar intumescence was dissected for tissue dissociation using mechanical methods (1). The resulting cell suspension was passed through stainless-steel meshes (140 and 70  $\mu\text{m}$ ) to remove myelin debris. Subsequently, different concentrations of Percoll solution were added to the cell suspension to separate glial and immune cells and centrifuge for 30 min— $400\times g$ — $4^\circ\text{C}$  (without a break) (2). Ex vivo stimulation was performed at previously separated layers at the interface using PMA, ionomycin, and brefeldin A for 3 h at  $37^\circ\text{C}$ — $5\% \text{CO}_2$  (3). Following stimulation, each layer interface was resuspended in a Wash B buffer for flow cytometry. The cell suspension was transferred from the cell culture to a 96-well plate, according to the specific antibody panel (4). For cell labeling, a combination of extracellular and intracellular antibodies was added to the cell suspension of each layer interface. Permeabilization and fixation were performed using the True-Nuclear Transcription Buffer Set (Biolegend), following the manufacturer’s recommendations (5). Cell acquisition was conducted using the NovoCyte flow cytometer (ACEA—Biosciences), ensuring a minimum of 10,000 events per tube. A cell blank tube was used as a control (6).

### Computational analysis—gate detection

Reliable data management is the groundwork of successful analysis, improving the reproducibility of experimental findings. In this way, we used k-means, a machine learning tool, to reduce the data dimension and semi-automatically detect the gate (see the computational schematic in Figure 3 after the elimination of doublets by NovoExpress software (version 1.6.2)).

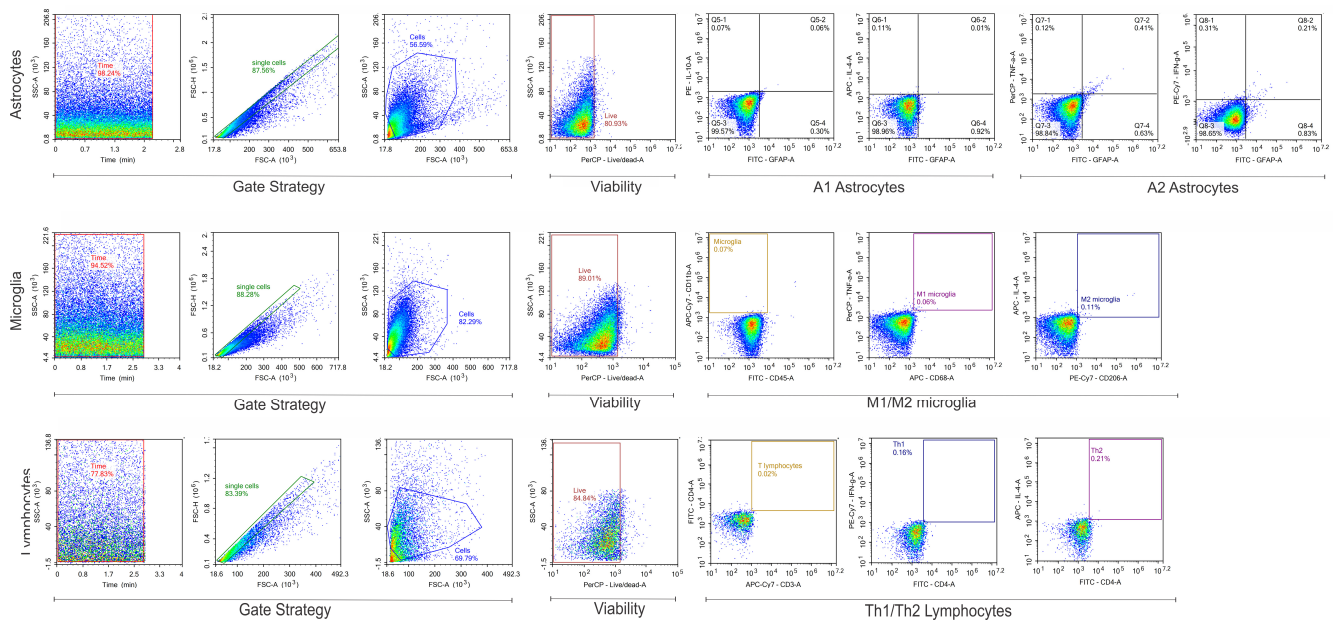


**Figure 2.** Determination of control gate: The time gate was set to start the analysis, following removing doublets at the single-cell gating. To analyze the cell phenotype, we established a control gate using unlabeled cells. Doublets were eliminated by segregating events based on FSC-A and FSC-H parameters. A two-dimensional plot of FSC-A vs. FSC-H was employed to visualize the doublet-free events, defining the “single cells” population. Subsequently, a dotplot combining complexity and size (FSC-A vs. SCA-A) was generated to determine the cell population. Cell viability was analyzed by negative cells from live/dead markers. To assess marker fluorescence, a quadrant was placed immediately after the final events of the population, ensuring all subsequent events exhibited positive marker signals. This strategy was applied at each layer interface.

The k-means clustering algorithm uses Voronoi diagrams, which are compounded by Voronoi cells, to group similar data points (cytometry events). For each Voronoi cell, the variance was computed, and the centroids were the mean of each geometric space present inside the original dataset. Debris was removed in Python by the single ellipse gate method implementation. A linear regression (Figures 3 and 4, blue lines) for five centroids was required to define the shape and position of the ellipse, which was defined by the following four parameters: width, height, angle, and coordinates of the center. Our method set the width as the Euclidean distance between the first and third centroids and the height as the Euclidean distance between the first and last centroid in the x and y coordinates. A 5% factor was applied to both width and height to include events close to the edge of the centroids. The angle of the ellipse was defined by the angular coefficient of the linear regression of the centroids. The center of the ellipse was set as the midpoint of the line segment formed by the linear regression function applied to the x-coordinate of the first and last centroids.

The computational method was tested for three cytometry datasets to reinforce the method’s applicability to semi-autonomous gates. Specifically, for the parameterization step, only 5 clusters (Figure 4A, red dot points) were enough to fit a manual gate determined by an expert in cytometry. We chose two more complex event distribution cytometry datasets for the validation step. The mathematical method implemented for the two validation datasets involved finding 10 (Figure 4B, red dot points) and 30 (Figure 4C, red dot points) clusters, respectively. The specific number of clusters was distinctive as a result of complex event distribution inside both datasets (Dataset 2–3). From these numbers of clusters, five were selected to apply to the method. This included centroids 1, 3, 6, 7, and 8 and 1, 14, 17, 21, and 23 for datasets 2 and 3, respectively. This interaction turned the mathematical method semi-automatic. We considered a valid result if the semi-

autonomous gate comprised at least 86% of the events of a manual gate determined by a specialist in cytometry.

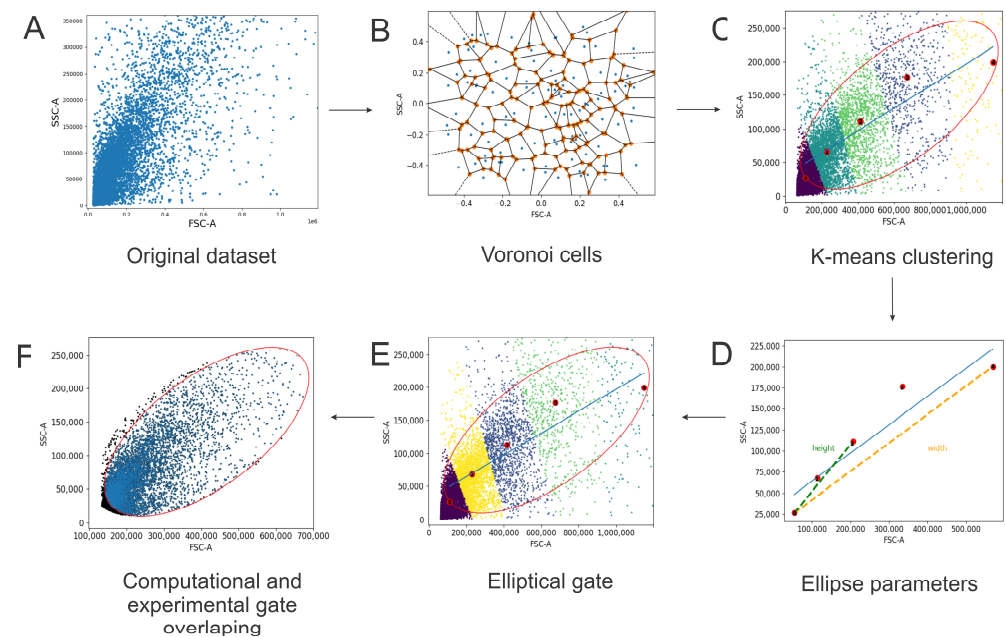


**Figure 3.** Computational schematic. Original cytometry dataset after removing doublets in blue dots (A). Determinations of Voronoi cells for K-means clustering (B) (five clusters are shown in Panel 3). The red dots indicate the five centroids of five clusters (purple, blue, green, yellow and ciano dots) (C,D). The green and yellow dashed lines represent the height and width of the ellipse, respectively (D). The blue line is the five centroids’ linear regression. The computational gate obtained by a mathematical method is shown in red after five clusters determinations (purple, ciano, yellow, and green dots) (E). Black dots indicate experimental events within the gate determined by an expert in cytometry analysis; blue dots indicate events within the computational gate (red ellipse) determined by our method (F).

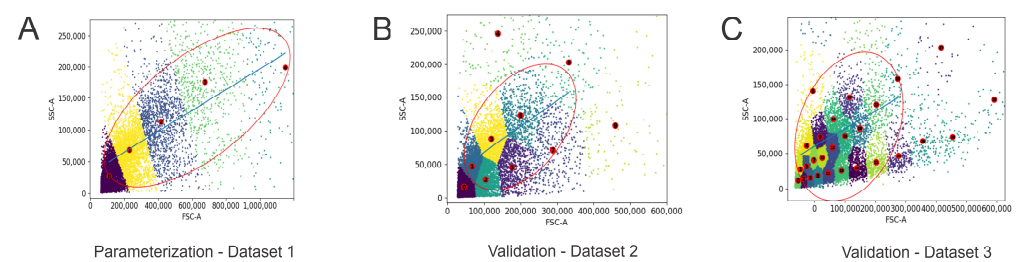


**Figure 4.** Parameterization and validation steps. Cytometry dataset 1 used for parameterization (A). Cytometry datasets 2 and 3 were used to validate the mathematical method Panels (B,C). Red dots indicate centroids; red ellipses are the gates; the blue lines represent the linear regression of the centroids; and the clusters are the event groups with different colors.

### 3. Results

#### 3.1. Isolation and Characterization of Glial and Immune Cells

The use of the Percoll gradient in different concentrations allows the isolation of glial and immune cells from the spinal cord. The first Percoll concentration (10%) concentrates myelin, avoiding the contamination of other layers. Following this, Percoll’s concentrations were used to isolate each cell type based on their size and complexity.

Thus, the 10/37 Percoll layer was enriched with astrocytes, the 37/50 Percoll layer presented a greater concentration of microglial cells, and the 50/70 Percoll layer had isolated lymphocytes.





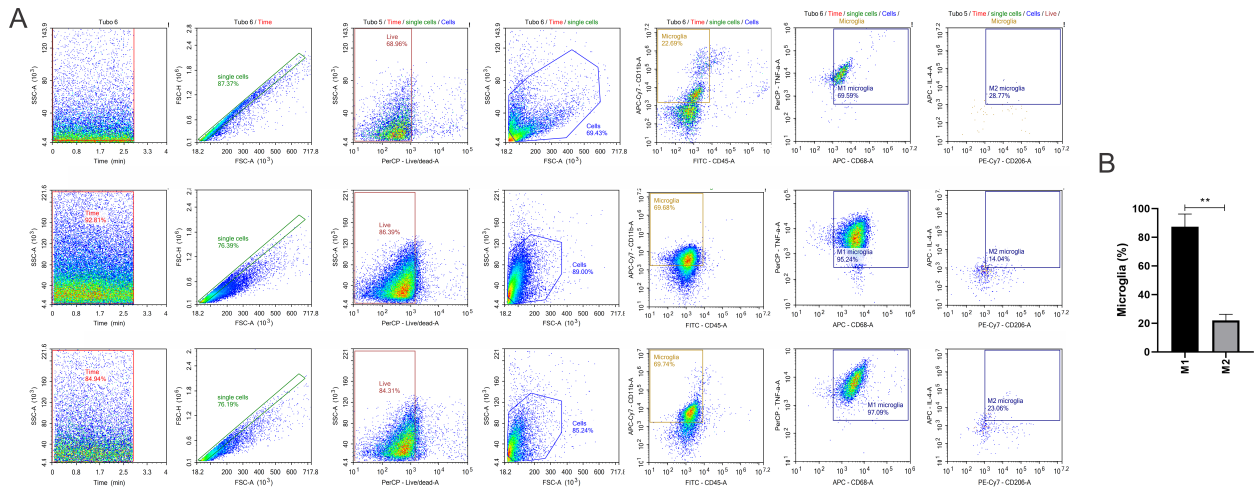


**Figure 6.** Microglia isolation in a triplicate experiment to show the reproducibility of the method. First, we removed readings of cells mixed with air bubbles through SSC-A vs. time, following the removal of doublets by single-cell analysis. Cell viability was set by live/dead vs. SSC-A so that a negative marker for cell death was used to further analyze the cell phenotype. Cells were separated in FSC-A vs. SCA-A to delimit the population for further analysis. Then, CD11b+CD45<sup>low</sup> was considered to analyze the microglial cells. The M1 profile was considered CD68+TNF- $\alpha$ +, and M2 was CD206+IL-4+ (A). The percentage of M1 and M2 subsets at the non-lesioned lumbar spinal cord (B). Unpaired *t* test, *p* < 0.005 (\*\*).

Isolating microglia from the normal spinal cord demonstrated pro-inflammatory promptness by secreting TNF- $\alpha$ , a hallmark of the M1 profile (Figure 6A,B). Of note, the number of CD11b+CD45<sup>low</sup> cells was about 50% in the 37/50 layer, which is considered as resting-state microglia (Figure 6A) (Supplementary Table S2). The viability test, using a live/dead method in the 37/50 layer, was greater than 80% (Figure 6B) (Supplementary Table S1).

Lastly, in the 50/70 layer, we isolated lymphocytes; then, they were separated into CD3+CD4+ positive cells to differentiate CD4+ T from CD8+ T lymphocytes, then Th1 and Th2 cells were analyzed by CD4+IFN- $\gamma$  and CD4+IL-4+ expression, respectively (Figure 7A). In this case, we also observed a pro-inflammatory preset by the higher percentage of Th1 cells at basal levels (Figure 7A,B) (Supplementary Table S2). The viability test, by using a live/dead method in the 50/70 layer, showed results greater than 50% after the isolation (Figure 7B) (Supplementary Table S1).

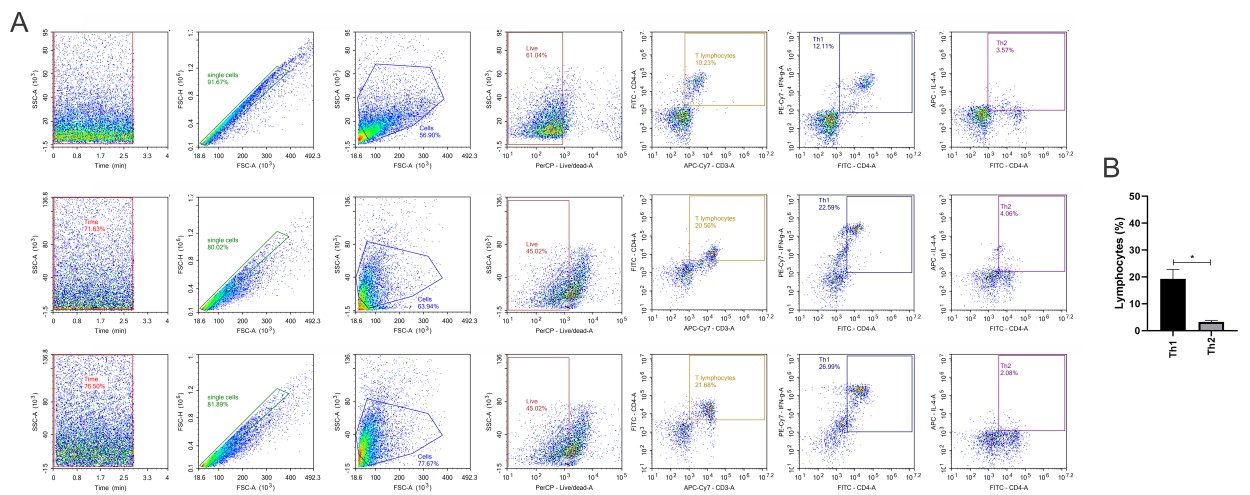


**Figure 7.** Lymphocyte isolation in triplicate. Cells were isolated at the 50/70-layer Percoll density gradient, and the population was delimited by FSC-A vs. SCA-A. Cell viability was set by live/dead vs. SSC-A so that a negative marker for cell death could be used to further analyze the cell phenotype.

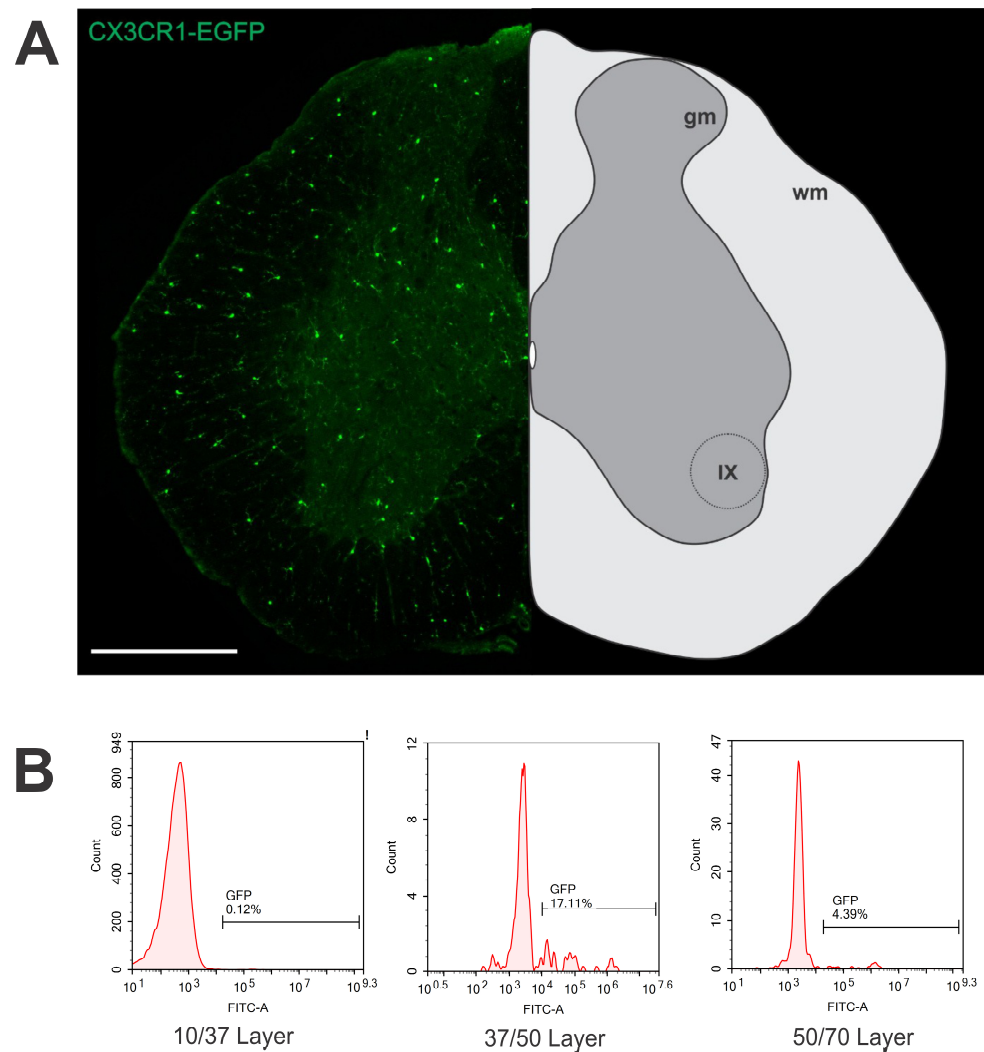


Then, T CD4 lymphocytes were phenotyped by expressing CD3+CD4+, and Th1 and Th2 lymphocytes were separated by the expression of IFN- $\gamma$  and IL-4, respectively (A). The percentage of Th1 and Th2 lymphocytes after the isolation (B). Unpaired *t* test,  $p < 0.05$  (\*).

### 3.2. Microglia Labeling from CX3CR1-EGFP Animals

To confirm the isolation protocol, we utilized CX3CR1-EGFP animals, which have fluorescent microglia. Frozen 12  $\mu\text{m}$  thick slides from the lumbar spinal cord were obtained and analyzed by immunofluorescence microscopy (Figure 8A). Transgenic EGFP fluorescence was detected and revealed an even distribution of microglial cells in the spinal cord gray matter (Figure 8A).

For the flow cytometry evaluation, Percoll gradient isolation was carried out, and cells from different layers were separated by the expression of EGFP. The results demonstrated that the highest frequency of positive cells was found in the 37/50 Percoll layer (17, 11%, Figure 8B). Considering that this value was reduced in comparison to the herein proposed phenotyping method (CD11b+CD45<sup>low</sup>), it is possible that the cell separation method partially depleted EGFP fluorescence. In turn, future experiments may consider the addition of an anti-EGFP antibody in the case of using transgenic fluorescent mice.

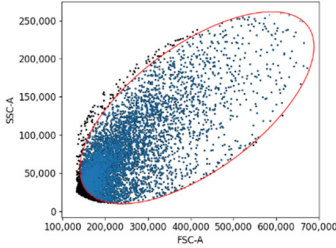
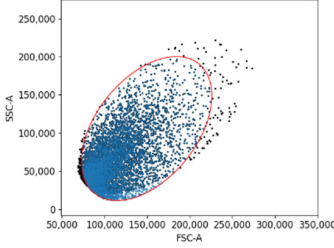
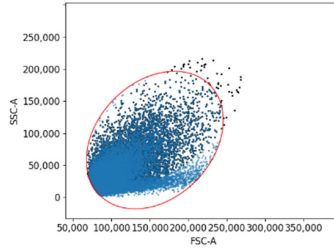


**Figure 8.** Immunofluorescence of microglia from CX3CR1-EGFP mouse lumbar spinal cord (A). GFP expression was evaluated in the 10/37, 37/50, and 50/70 layers (B), demonstrating that most of the fluorescent cells were present in the 37/50 interface. gm = gray matter; wm: white matter; IX = lamina IX of Rexed.

### 3.3. Computational Analysis of Gate Strategy

To further improve the flow cytometry evaluation, we confirmed the manual gate method with a semi-automatic mathematical approach. Table 2 shows the manual (black dots) and computational (blue dots and red ellipses) gates overlapping. The similarity between the percentage of events inside the manual and computational gates ( $7.19\% \pm 5.27\%$ , mean  $\pm$  STD) indicates that the present method is reliable and could be replicated in later studies.

**Table 2.** Experimental (black dots) and computational (blue dots and red ellipses) gate overlap. The difference between the percentages of events inside the semi-autonomous and manual (determined by an expert in flow cytometry) gates was  $7.19\% \pm 5.27\%$  (mean  $\pm$  STD).

Steps	Parameterization	Validation	
Datasets	1	2	3
			
Computational gate (%)	59.47%	46.92%	62.14%
Experimental gate (%)	75.75%	46.50%	54.28%

To enhance flow cytometry evaluation, we validated the manual gating method using a semi-automatic mathematical approach. This involved employing the K-means algorithm to partition cytometry data into  $k$  clusters of equal variances, with each observation assigned to the cluster with the nearest mean. This process minimized the within-cluster sum-of-squares, also known as inertia or distortion, which gauges the compactness of the clusters. The K-means algorithm operates as follows:

1. **Initialization:**  $k$  initial cluster centroids are randomly selected from the cytometry dataset.
2. **Assignment:** each data point is assigned to the nearest cluster centroid based on a distance metric, usually the Euclidean distance.
3. **Update Centroids:** the centroids of the clusters are recalculated by computing the mean of all data points assigned to each cluster.
4. **Repeat:** steps 2 and 3 are iterated until convergence is achieved, meaning the cluster assignments no longer change significantly or a specified number of iterations is reached.
5. **Finalization:** upon convergence, the algorithm produces the final cluster assignments and centroids.

Table 2 shows the overlap between manual gates (depicted as black dots) and computational gates (represented by blue dots and red ellipses). The similarity in the percentage of events inside the manual and computational gates ( $7.19\% \pm 5.27\%$ , mean  $\pm$  standard deviation) suggests the reliability of the present method, which can be replicated in future studies.

The computational gates are entirely open-source, developed in Python 3.5, leveraging scikit-learn libraries built on NumPy, SciPy, and matplotlib. For a comprehensive understanding of gate detection, refer to the “Computational analysis—gate detection” section of the Methodology.

#### 4. Discussion

Aging, injury, and disease trigger inflammatory responses in the CNS microenvironment that may result in neuronal loss and maladaptive plasticity, leading to dysfunction and irreversible conditions [9,53,54]. Pro-inflammatory cytokines released by astrocytes trigger transcriptional shifts, which may alter synaptic activity, resulting in behavioral and cognitive alterations [55–57]. Furthermore, microglia also play a pivotal role, developing the first immune response acutely after injury and disease [34]. Thus, understanding the cellular changes in the CNS is key to the development of new approaches to treatments that can be more successful than those currently available.

Glial and immune activation in response to injury is a complex process that involves the interplay of a myriad of molecules [34]. Cytokines, in particular, are of great importance to signal cell polarization towards a pro- or anti-inflammatory profile [34]. Herein, we demonstrate a flow cytometry protocol to analyze glial and immune cells from the spinal cord. Such a straightforward approach may facilitate the upscaling of cell profiling in the CNS, allowing a wider view of inflammatory/infection processes. Furthermore, a mathematical method for finding the initial gates is proposed to make the cytometric analysis easier and faster.

The use of Percoll gradient isolation is a powerful technique that has also been used in other organs, like the blood, spleen, and lymph nodes [58–62]. At the spinal cord, we were able to analyze different cell types, such as microglia, astrocytes, and lymphocytes. One advantage of Percoll gradient isolation is that it is a gentle and non-destructive technique that can preserve the viability and function of isolated cells. Several articles present different protocols for spinal cord flow cytometry; therefore, there is no unique protocol to isolate glial and immune cells from the spinal cord.

Bergmann and colleagues (1999) described how the mononuclear cells from CNS could be separated by the Percoll density gradient. They observed that CD8 T lymphocytes were isolated from the Percoll 30/70 interface [63]. Furthermore, Becher et al. described the separation of CNS-resident cells, such as microglia and macrophages, in the Percoll 37/70 layer [64,65]. In the same way, Cardona et al. also described microglia separation utilizing the Percoll 37/70 layer [66]. Also, utilizing mononuclear cells as the cell of interest, Pino and colleagues (2011) utilized Percoll 30/70 to analyze the cells from the spinal cord. In all cases, the use of enzymatic procedures was avoided to minimize cell death and, consequently, result in a greater number of viable cells, which can be utilized for further characterization [67,68]. Juedes & Ruddle (2001) utilized the digestion enzymatic protocol with collagenase II and the discontinuous Percoll gradient to isolate mononuclear cells [69]. Agalave et al. (2020) demonstrated that by utilizing Percoll 37/50 and 50/70, it was possible to separate astrocytes and microglia from the spinal cord [68].

The present protocol is optimized to separate astrocytes, microglia, and lymphocytes from the spinal cord at the same time by adding Percoll 10% to separate myelin from the glial and immune cells. Thus, we isolated astrocytes from the Percoll 10/37 layer, microglia from the Percoll 37/50 layer, and lymphocytes from the Percoll 50/70 layer. We also certified that our separation was reliable by demonstrating that most of the microglia in CX3CR1 animals were found in the Percoll 37/50 layer.

In the present study, unlesioned spinal cord tissue was used so that cells were isolated in basal conditions without priming or polarization. Nevertheless, an important observation is that microglial cells, astrocytes, and lymphocytes displayed, in greater percentages, markers of pro-inflammatory response. Such pre-inflammatory stages can be useful to maintain the homeostasis of the CNS as they can facilitate the response to injury or disease [70,71]. A recent study from our group employed flow cytometry phenotyping in SOD1G93A animals (an ALS experimental model), observing a shift towards an anti-inflammatory response in microglial cells (M2 profile) after IFN-beta treatment [72], demonstrating that the above-mentioned pre-inflammatory stage in basal levels can be changed upon pharmacological therapy [72].

In addition to the cell separation method proposed, a mathematical method is suggested to facilitate the manual gate selection during cytometric analysis. Despite other efforts in the computational cytometry area [49,50], our mathematical method involves a relatively simple strategy, using the Euclidean distance of points (K-means centroids of the clusters), which implies the absence of the need for extremely powerful computational power.

The proposed cell separation method is complemented by a mathematical approach aimed at streamlining manual gate selection in cytometric analysis. Despite other efforts in the computational cytometry area [49,50], our method relies on a relatively simple strategy: utilizing the K-means centroids of clusters and the Euclidean distance of points, eliminating the need for high computational power. Two critical factors significantly contributed to enhancing the accuracy of semi-autonomous gate detection. Firstly, K-means effectively reduced the dimensionality of cytometry data, which was similarly proposed by [50]. Nevertheless, our mathematical method involved human interactions for the selection of a correct and concise set of centroids for the Euclidean distance calculation, which is different from the autonomous gate detection proposed by [49]. Secondly, the straightforward Euclidean distance calculation played a crucial and original advantage in the process of defining the elliptical gate parameters. This approach achieved an 86% accuracy rate compared to the manual gate detection performed using NovoExpress software (version 1.6.2). Notably, this level of accuracy was attained within 28 s on a Dell XPS 13 9360 notebook, featuring an Intel(R) Core(TM) i7-7500U CPU @ 2.70 GHz, with two cores and four logical processors. The adoption of semi-autonomous gating not only expedites the analysis but also lays the groundwork for integrating gate selection methods into freely accessible cytometry software in the future. This improvement ensures the reproducibility and reliability of flow cytometry analysis.

In conclusion, the present cell isolation protocol allows for a more comprehensive study of the glial and immune response. It is easier and less expensive to isolate glial cells and lymphocytes from the spinal cord using this method. The broad screening potential of flow cytometry allows for the phenotyping of cells, which may facilitate advances in the understanding of many diseases and injuries, as well as the identification of specific therapeutic targets that may be translated into the clinic in the future.

**Supplementary Materials:** The following supporting information can be downloaded at: <https://www.mdpi.com/article/10.3390/neuroglia5020010/s1>, Table S1: Viability summary of each sample into different layers interface after Percoll gradient isolation. Table S2: Statistical analysis of cell polarization after flow cytometry data analysis.

**Author Contributions:** L.d.O.C.: animal experiments, data collection, analysis and interpretation of data, design, and construction of the article. M.T.C.: animal experiments and data collection. D.E.d.C.M.: computational analysis and interpretation. L.P.C.: Histological analysis from CXCR-EGFP animals. A.L.R.d.O.: supervision, design, and concept of the article, interpretation of data, and critical revision. All authors have read and agreed to the published version of the manuscript.

**Funding:** This research was funded by CNPq (National Council for Scientific and Technological Development) #140027/2020-3 and FAPESP (Sao Paulo Research Foundation) #2018/05006-0).

**Institutional Review Board Statement:** The animal study protocol was approved by the National Council for Animal Experimentation Control (CONCEA—Brazil and were approved by the Institutional Ethics Committee on the Use of Animals—CEUA/IB/UNICAMP, protocol n° 5327-1/2019).

**Acknowledgments:** We thank Heitor Sanchez Fernandes for the computational analysis and interpretation assistance for gate detection.

**Conflicts of Interest:** The authors declare no conflicts of interest.

## References

1. Gogoleva, V.S.; Drutskaya, M.S.; Atretkhany, K.S. The Role of Microglia in the Homeostasis of the Central Nervous System and Neuroinflammation. *Mol. Biol.* **2019**, *53*, 790–798. [[CrossRef](#)] [[PubMed](#)]
2. Sofroniew, M.V.; Vinters, H.V. Astrocytes: Biology and pathology. *Acta Neuropathol.* **2010**, *119*, 7–35. [[CrossRef](#)] [[PubMed](#)]
3. Farina, C.; Aloisi, F.; Meinl, E. Astrocytes are active players in cerebral innate immunity. *Trends Immunol.* **2007**, *28*, 138–145. [[CrossRef](#)]
4. Verkhatsky, A.; Nedergaard, M. Physiology of Astroglia. *Physiol. Rev.* **2018**, *98*, 239–389. [[CrossRef](#)] [[PubMed](#)]
5. Magistretti, P.J.; Allaman, I. Lactate in the brain: From metabolic end-product to signalling molecule. *Nat. Rev. Neurosci.* **2018**, *19*, 235–249. [[CrossRef](#)] [[PubMed](#)]
6. MacVicar, B.A.; Newman, E.A. Astrocyte regulation of blood flow in the brain. *Cold Spring Harb. Perspect. Biol.* **2015**, *7*, a020388. [[CrossRef](#)] [[PubMed](#)]
7. Allen, N.J.; Eroglu, C. Cell Biology of Astrocyte-Synapse Interactions. *Neuron* **2017**, *96*, 697–708. [[CrossRef](#)] [[PubMed](#)]
8. Khakh, B.S. Astrocyte-Neuron Interactions in the Striatum: Insights on Identity, Form, and Function. *Trends Neurosci.* **2019**, *42*, 617–630. [[CrossRef](#)]
9. Kruyer, A. Astrocyte Heterogeneity in Regulation of Synaptic Activity. *Cells* **2022**, *11*, 3135. [[CrossRef](#)]
10. Wrobel, M.R.; Sundararaghavan, H.G. Biomaterial Cues to Direct a Pro-regenerative Phenotype in Macrophages and Schwann Cells. *Neuroscience* **2018**, *376*, 172–187. [[CrossRef](#)]
11. Liddelow, S.A.; Guttenplan, K.A.; Clarke, L.E.; Bennett, F.C.; Bohlen, C.J.; Schirmer, L.; Bennett, M.L.; Münch, A.E.; Chung, W.S.; Peterson, T.C.; et al. Neurotoxic reactive astrocytes are induced by activated microglia. *Nature* **2017**, *541*, 481–487. [[CrossRef](#)] [[PubMed](#)]
12. Walker, C.D.; Risher, W.C.; Risher, M.L. Regulation of Synaptic Development by Astrocyte Signaling Factors and Their Emerging Roles in Substance Abuse. *Cells* **2020**, *9*, 297. [[CrossRef](#)]
13. Zamanian, J.L.; Xu, L.; Foo, L.C.; Nouri, N.; Zhou, L.; Giffard, R.G.; Barres, B.A. Genomic analysis of reactive astrogliosis. *J. Neurosci.* **2012**, *32*, 6391–6410. [[CrossRef](#)] [[PubMed](#)]
14. Anderson, M.A.; Burda, J.E.; Ren, Y.; Ao, Y.; O’Shea, T.M.; Kawaguchi, R.; Coppola, G.; Khakh, B.S.; Deming, T.J.; Sofroniew, M.V. Astrocyte scar formation aids central nervous system axon regeneration. *Nature* **2016**, *532*, 195–200. [[CrossRef](#)]
15. Lian, H.; Yang, L.; Cole, A.; Sun, L.; Chiang, A.C.; Fowler, S.W.; Shim, D.J.; Rodriguez-Rivera, J.; Taglialatela, G.; Jankowsky, J.L.; et al. NFκB-activated astroglial release of complement C3 compromises neuronal morphology and function associated with Alzheimer’s disease. *Neuron* **2015**, *85*, 101–115. [[CrossRef](#)] [[PubMed](#)]
16. Colonna, M.; Butovsky, O. Microglia Function in the Central Nervous System During Health and Neurodegeneration. *Annu. Rev. Immunol.* **2017**, *35*, 441–468. [[CrossRef](#)]
17. Orihuela, R.; McPherson, C.A.; Harry, G.J. Microglial M1/M2 polarization and metabolic states. *Br. J. Pharmacol.* **2016**, *173*, 649–665. [[CrossRef](#)]
18. Sica, A.; Mantovani, A. Macrophage plasticity and polarization: In vivo veritas. *J. Clin. Investig.* **2012**, *122*, 787–795. [[CrossRef](#)]
19. Tang, Y.; Le, W. Differential Roles of M1 and M2 Microglia in Neurodegenerative Diseases. *Mol. Neurobiol.* **2016**, *53*, 1181–1194. [[CrossRef](#)]
20. Nguyen, H.M.; Grössinger, E.M.; Horiuchi, M.; Davis, K.W.; Jin, L.W.; Maezawa, I.; Wulff, H. Differential Kv1.3, KCa3.1, and Kir2.1 expression in “classically” and “alternatively” activated microglia. *Glia* **2017**, *65*, 106–121. [[CrossRef](#)]
21. Durafourt, B.A.; Moore, C.S.; Blain, M.; Antel, J.P. Isolating, culturing, and polarizing primary human adult and fetal microglia. *Methods Mol. Biol.* **2013**, *1041*, 199–211. [[CrossRef](#)] [[PubMed](#)]
22. Martinez, F.O.; Helming, L.; Gordon, S. Alternative activation of macrophages: An immunologic functional perspective. *Annu. Rev. Immunol.* **2009**, *27*, 451–483. [[CrossRef](#)]
23. Saijo, K.; Glass, C.K. Microglial cell origin and phenotypes in health and disease. *Nat. Rev. Immunol.* **2011**, *11*, 775–787. [[CrossRef](#)] [[PubMed](#)]
24. Hu, X.; Li, P.; Guo, Y.; Wang, H.; Leak, R.K.; Chen, S.; Gao, Y.; Chen, J. Microglia/macrophage polarization dynamics reveal novel mechanism of injury expansion after focal cerebral ischemia. *Stroke* **2012**, *43*, 3063–3070. [[CrossRef](#)]
25. Cherry, J.D.; Olschowka, J.A.; O’Banion, M.K. Neuroinflammation and M2 microglia: The good, the bad, and the inflamed. *J. Neuroinflamm.* **2014**, *11*, 98. [[CrossRef](#)]
26. Mazzer, P.Y.; Barbieri, C.H.; Mazzer, N.; Fazan, V.P. Morphologic and morphometric evaluation of experimental acute crush injuries of the sciatic nerve of rats. *J. Neurosci. Methods* **2008**, *173*, 249–258. [[CrossRef](#)]
27. Zrzavy, T.; Schwaiger, C.; Wimmer, I.; Berger, T.; Bauer, J.; Butovsky, O.; Schwab, J.M.; Lassmann, H.; Höftberger, R. Acute and non-resolving inflammation associate with oxidative injury after human spinal cord injury. *Brain* **2021**, *144*, 144–161. [[CrossRef](#)]
28. Fan, H.; Zhang, K.; Shan, L.; Kuang, F.; Chen, K.; Zhu, K.; Ma, H.; Ju, G.; Wang, Y.Z. Reactive astrocytes undergo M1 microglia/macrophages-induced necroptosis in spinal cord injury. *Mol. Neurodegener.* **2016**, *11*, 14. [[CrossRef](#)] [[PubMed](#)]
29. Valori, C.F.; Brambilla, L.; Martorana, F.; Rossi, D. The multifaceted role of glial cells in amyotrophic lateral sclerosis. *Cell. Mol. Life Sci.* **2014**, *71*, 287–297. [[CrossRef](#)]
30. Zürcher, N.R.; Loggia, M.L.; Lawson, R.; Chonde, D.B.; Izquierdo-Garcia, D.; Yasek, J.E.; Akeju, O.; Catana, C.; Rosen, B.R.; Cudkovicz, M.E.; et al. Increased in vivo glial activation in patients with amyotrophic lateral sclerosis: Assessed with [(11)C]-PBR28. *Neuroimage Clin.* **2015**, *7*, 409–414. [[CrossRef](#)]



31. Luo, C.; Jian, C.; Liao, Y.; Huang, Q.; Wu, Y.; Liu, X.; Zou, D. The role of microglia in multiple sclerosis. *Neuropsychiatr. Dis. Treat.* **2017**, *13*, 1661–1667. [[CrossRef](#)]
32. Napoli, I.; Neumann, H. Protective effects of microglia in multiple sclerosis. *Exp. Neurol.* **2010**, *225*, 24–28. [[CrossRef](#)]
33. Shih, R.H.; Wang, C.Y.; Yang, C.M. NF-kappaB Signaling Pathways in Neurological Inflammation: A Mini Review. *Front. Mol. Neurosci.* **2015**, *8*, 77. [[CrossRef](#)] [[PubMed](#)]
34. Gaudet, A.D.; Fonken, L.K. Glial Cells Shape Pathology and Repair after Spinal Cord Injury. *Neurotherapeutics* **2018**, *15*, 554–577. [[CrossRef](#)] [[PubMed](#)]
35. Janda, E.; Boi, L.; Carta, A.R. Microglial Phagocytosis and Its Regulation: A Therapeutic Target in Parkinson's Disease? *Front. Mol. Neurosci.* **2018**, *11*, 144. [[CrossRef](#)]
36. Bellver-Landete, V.; Bretheau, F.; Mailhot, B.; Vallières, N.; Lessard, M.; Janelle, M.E.; Vernoux, N.; Tremblay, M.; Fuehrmann, T.; Shoichet, M.S.; et al. Microglia are an essential component of the neuroprotective scar that forms after spinal cord injury. *Nat. Commun.* **2019**, *10*, 518. [[CrossRef](#)] [[PubMed](#)]
37. Bundesen, L.Q.; Scheel, T.A.; Bregman, B.S.; Kromer, L.F. Ephrin-B2 and EphB2 regulation of astrocyte-meningeal fibroblast interactions in response to spinal cord lesions in adult rats. *J. Neurosci.* **2003**, *23*, 7789–7800. [[CrossRef](#)]
38. Soderblom, C.; Luo, X.; Blumenthal, E.; Bray, E.; Lyapichev, K.; Ramos, J.; Krishnan, V.; Lai-Hsu, C.; Park, K.K.; Tsoulfas, P.; et al. Perivascular fibroblasts form the fibrotic scar after contusive spinal cord injury. *J. Neurosci.* **2013**, *33*, 13882–13887. [[CrossRef](#)]
39. Tran, A.P.; Warren, P.M.; Silver, J. New insights into glial scar formation after spinal cord injury. *Cell Tissue Res.* **2022**, *387*, 319–336. [[CrossRef](#)]
40. Gadani, S.P.; Walsh, J.T.; Lukens, J.R.; Kipnis, J. Dealing with Danger in the CNS: The Response of the Immune System to Injury. *Neuron* **2015**, *87*, 47–62. [[CrossRef](#)]
41. Greenhalgh, A.D.; David, S. Differences in the phagocytic response of microglia and peripheral macrophages after spinal cord injury and its effects on cell death. *J. Neurosci.* **2014**, *34*, 6316–6322. [[CrossRef](#)] [[PubMed](#)]
42. Ma, M.; Wei, T.; Boring, L.; Charo, I.F.; Ransohoff, R.M.; Jakeman, L.B. Monocyte recruitment and myelin removal are delayed following spinal cord injury in mice with CCR2 chemokine receptor deletion. *J. Neurosci. Res.* **2002**, *68*, 691–702. [[CrossRef](#)] [[PubMed](#)]
43. Ehrhard, P.B.; Erb, P.; Graumann, U.; Otten, U. Expression of nerve growth factor and nerve growth factor receptor tyrosine kinase Trk in activated CD4-positive T-cell clones. *Proc. Natl. Acad. Sci. USA* **1993**, *90*, 10984–10988. [[CrossRef](#)] [[PubMed](#)]
44. Kerschensteiner, M.; Gallmeier, E.; Behrens, L.; Leal, V.V.; Misgeld, T.; Klinkert, W.E.; Kolbeck, R.; Hoppe, E.; Oropeza-Wekerle, R.L.; Bartke, I.; et al. Activated human T cells, B cells, and monocytes produce brain-derived neurotrophic factor in vitro and in inflammatory brain lesions: A neuroprotective role of inflammation? *J. Exp. Med.* **1999**, *189*, 865–870. [[CrossRef](#)] [[PubMed](#)]
45. Kobayashi, S.; Yoshizawa, H.; Yamada, S. Pathology of lumbar nerve root compression. Part 2: Morphological and immunohistochemical changes of dorsal root ganglion. *J. Orthop. Res.* **2004**, *22*, 180–188. [[CrossRef](#)] [[PubMed](#)]
46. Krassioukov, A. Autonomic function following cervical spinal cord injury. *Respir. Physiol. Neurobiol.* **2009**, *169*, 157–164. [[CrossRef](#)] [[PubMed](#)]
47. Anderson, K.D. Targeting recovery: Priorities of the spinal cord-injured population. *J. Neurotrauma* **2004**, *21*, 1371–1383. [[CrossRef](#)]
48. Thuret, S.; Moon, L.D.; Gage, F.H. Therapeutic interventions after spinal cord injury. *Nat. Rev. Neurosci.* **2006**, *7*, 628–643. [[CrossRef](#)] [[PubMed](#)]
49. Burton, R.J.; Ahmed, R.; Cuff, S.M.; Baker, S.; Artemiou, A.; Eberl, M. CytoPy: An autonomous cytometry analysis framework. *PLoS Comput. Biol.* **2021**, *17*, e1009071. [[CrossRef](#)]
50. Wong, N.; Kim, D.; Robinson, Z.; Huang, C.; Conboy, I.M. K-means quantization for a web-based open-source flow cytometry analysis platform. *Sci. Rep.* **2021**, *11*, 6735. [[CrossRef](#)]
51. Jung, S.; Aliberti, J.; Graemmel, P.; Sunshine, M.J.; Kreutzberg, G.W.; Sher, A.; Littman, D.R. Analysis of fractalkine receptor CX(3)CR1 function by targeted deletion and green fluorescent protein reporter gene insertion. *Mol. Cell. Biol.* **2000**, *20*, 4106–4114. [[CrossRef](#)] [[PubMed](#)]
52. Escartin, C.; Galea, E.; Lakatos, A.; O'Callaghan, J.P.; Petzold, G.C.; Serrano-Pozo, A.; Steinhäuser, C.; Volterra, A.; Carmignoto, G.; Agarwal, A.; et al. Reactive astrocyte nomenclature, definitions, and future directions. *Nat. Neurosci.* **2021**, *24*, 312–325. [[CrossRef](#)] [[PubMed](#)]
53. Lawal, O.; Ulloa Severino, F.P.; Eroglu, C. The role of astrocyte structural plasticity in regulating neural circuit function and behavior. *Glia* **2022**, *70*, 1467–1483. [[CrossRef](#)] [[PubMed](#)]
54. Hassanzadeh, S.; Jalessi, M.; Jameie, S.B.; Khanmohammadi, M.; Bagher, Z.; Namjoo, Z.; Davachi, S.M. More attention on glial cells to have better recovery after spinal cord injury. *Biochem. Biophys. Rep.* **2021**, *25*, 100905. [[CrossRef](#)] [[PubMed](#)]
55. Sofroniew, M.V. Multiple roles for astrocytes as effectors of cytokines and inflammatory mediators. *Neuroscientist* **2014**, *20*, 160–172. [[CrossRef](#)] [[PubMed](#)]
56. Xu, P.; Huang, X.; Niu, W.; Yu, D.; Zhou, M.; Wang, H. Metabotropic glutamate receptor 5 upregulation of  $\gamma$ -aminobutyric acid transporter 3 expression ameliorates cognitive impairment after traumatic brain injury in mice. *Brain Res. Bull.* **2022**, *183*, 104–115. [[CrossRef](#)] [[PubMed](#)]
57. Ben Haim, L.; Carrillo-de Sauvage, M.A.; Ceyzériat, K.; Escartin, C. Elusive roles for reactive astrocytes in neurodegenerative diseases. *Front. Cell. Neurosci.* **2015**, *9*, 278. [[CrossRef](#)]

58. Herman, K.D.; Rahman, A.; Prince, L.R. Isolation and High Throughput Flow Cytometric Apoptosis Assay of Human Neutrophils to Enable Compound Library Screening. *Bio-Protocol* **2020**, *10*, e3640. [[CrossRef](#)] [[PubMed](#)]
59. Bloch, E.M.; Branch, H.A.; Sakac, D.; Leger, R.M.; Branch, D.R. Differential red blood cell age fractionation and Band 3 phosphorylation distinguish two different subtypes of warm autoimmune hemolytic anemia. *Transfusion* **2020**, *60*, 1856–1866. [[CrossRef](#)]
60. Safavi, F.; Thome, R.; Li, Z.; Zhang, G.X.; Rostami, A. Dimethyl fumarate suppresses granulocyte macrophage colony-stimulating factor-producing Th1 cells in CNS neuroinflammation. *Neurol. Neuroimmunol. Neuroinflamm.* **2020**, *7*, e729. [[CrossRef](#)]
61. Pacella, I.; Grimaldi, A.; Piconese, S. Assessment of lipid load in tumor-infiltrating Tregs by flow cytometry. *Methods Enzymol.* **2020**, *632*, 283–294. [[CrossRef](#)] [[PubMed](#)]
62. Bombeiro, A.L.; Santini, J.C.; Thomé, R.; Ferreira, E.R.; Nunes, S.L.; Moreira, B.M.; Bonet, I.J.; Sartori, C.R.; Verinaud, L.; Oliveira, A.L. Enhanced Immune Response in Immunodeficient Mice Improves Peripheral Nerve Regeneration Following Axotomy. *Front. Cell. Neurosci.* **2016**, *10*, 151. [[CrossRef](#)]
63. Bergmann, C.C.; Altman, J.D.; Hinton, D.; Stohlman, S.A. Inverted immunodominance and impaired cytolytic function of CD8+ T cells during viral persistence in the central nervous system. *J. Immunol.* **1999**, *163*, 3379–3387. [[CrossRef](#)]
64. Becher, B.; Durell, B.G.; Noelle, R.J. IL-23 produced by CNS-resident cells controls T cell encephalitogenicity during the effector phase of experimental autoimmune encephalomyelitis. *J. Clin. Invest.* **2003**, *112*, 1186–1191. [[CrossRef](#)] [[PubMed](#)]
65. Becher, B.; Durell, B.G.; Miga, A.V.; Hickey, W.F.; Noelle, R.J. The clinical course of experimental autoimmune encephalomyelitis and inflammation is controlled by the expression of CD40 within the central nervous system. *J. Exp. Med.* **2001**, *193*, 967–974. [[CrossRef](#)] [[PubMed](#)]
66. Cardona, A.E.; Huang, D.; Sasse, M.E.; Ransohoff, R.M. Isolation of murine microglial cells for RNA analysis or flow cytometry. *Nat. Protoc.* **2006**, *1*, 1947–1951. [[CrossRef](#)]
67. Pino, P.A.; Cardona, A.E. Isolation of brain and spinal cord mononuclear cells using percoll gradients. *J. Vis. Exp.* **2011**, *48*, e2348. [[CrossRef](#)] [[PubMed](#)]
68. Agalave, N.M.; Lane, B.T.; Mody, P.H.; Szabo-Pardi, T.A.; Burton, M.D. Isolation, culture, and downstream characterization of primary microglia and astrocytes from adult rodent brain and spinal cord. *J. Neurosci. Methods* **2020**, *340*, 108742. [[CrossRef](#)]
69. Juedes, A.E.; Ruddle, N.H. Resident and infiltrating central nervous system APCs regulate the emergence and resolution of experimental autoimmune encephalomyelitis. *J. Immunol.* **2001**, *166*, 5168–5175. [[CrossRef](#)]
70. Całkosiński, I.; Dobrzyński, M.; Całkosińska, M.; Seweryn, E.; Bronowicka-Szydełko, A.; Dzierżba, K.; Ceremuga, I.; Gamian, A. Characterization of an inflammatory response. *Postep. Hig. Med. Dosw. Online* **2009**, *63*, 395–408.
71. Shaw, A.C.; Goldstein, D.R.; Montgomery, R.R. Age-dependent dysregulation of innate immunity. *Nat. Rev. Immunol.* **2013**, *13*, 875–887. [[CrossRef](#)] [[PubMed](#)]
72. Tomiyama, A.; Cartarozzi, L.P.; de Oliveira Coser, L.; Chiarotto, G.B.; Oliveira, A.L.R. Neuroprotection by upregulation of the major histocompatibility complex class I (MHC I) in SOD1(G93A) mice. *Front. Cell. Neurosci.* **2023**, *17*, 1211486. [[CrossRef](#)] [[PubMed](#)]

**Disclaimer/Publisher’s Note:** The statements, opinions and data contained in all publications are solely those of the individual author(s) and contributor(s) and not of MDPI and/or the editor(s). MDPI and/or the editor(s) disclaim responsibility for any injury to people or property resulting from any ideas, methods, instructions or products referred to in the content.